

Electronic Transport Properties of 1,1'-Ferrocene Dicarboxylic Acid Linked to Al(111) Electrodes

Cristian Morari,^{†,*} Ivan Rungger,[§] Alexandre R. Rocha,^{§,⊥,¶} Stefano Sanvito,[§] Sorin Melinte,[†] and Gian-Marco Rignanesi^{†,*,#}

[†]Research Center on Microscopic and Nanoscopic Electronic Devices and Materials (CERMIN), Université Catholique de Louvain, 1348 Louvain-la-Neuve, Belgium, [‡]National Institute for Research and Development of Isotopic and Molecular Technologies (NIRDIMT), 65-103 Donath, Ro-400293, Cluj-Napoca, Romania, [§]School of Physics and CRANN, Trinity College, Dublin 2, Ireland, [⊥]Instituto de Física, Universidade de São Paulo, Caixa Postal 66318, 05315-970 São Paulo, São Paulo, Brazil, [¶]Centro de Ciências Naturais e Humanas, Universidade Federal do, ABC, 09090-400 Santo André, São Paulo, Brazil, and [#]European Theoretical Spectroscopy Facility (ETSF)

In its first stages of development, molecular electronics aimed at manufacturing molecular analogs to wires and switches, and conjugated molecules emerged as the main candidates to replace their inorganic counterparts.^{1–11} Today, molecular properties such as charge, spin, and conformation that are at the heart of experimental strategies to design advanced molecular devices^{12–16} and compounds including transition metal atoms receive weighty theoretical attention.

Ferrocene is the prototypical metal-locene. It consists of two cyclopentadienyl rings bound at the opposite sides of a central iron atom. It can present either the eclipsed (D_{5h} symmetry) or the staggered (D_{5d} symmetry) conformation, as illustrated in Figure 1a. At equilibrium, ferrocene is eclipsed while the staggered conformation constitutes the saddle-point to the internal rotation of the ligand rings. The energy difference between the two conformations is only a few tenths of meV so that, at room temperature, the two cyclopentane rings are almost free to rotate.¹⁷ Ferrocene derivatives represent a unique opportunity for conductance switching mainly due to their redox properties.^{18–22} Moreover the large spin polarization of ferrocene nanowires²³ and of metallocenes of the same family²⁴ can be exploited for realizing spin-polarizers at the molecular level.

Recently, a negative differential resistance has been observed for ferrocenyl-undecanethiolate self-assembled monolayers¹⁹ on Au(111) surfaces. By using ferrocene derivatives monolayers, planar tunnel junctions were demonstrated to

ABSTRACT The electronic transport properties of the 1,1'-ferrocene dicarboxylic acid sandwiched between Al(111) electrodes are studied using first-principles methods. The transmission spectra and the current–voltage characteristics are computed for various two-terminal device models and their relation with the electronic structure of the molecule is thoroughly discussed. The current–voltage characteristics are asymmetric, spin-independent, and vary with the anchoring structure of the molecule to the electrodes. A fine-tuning of the molecular conductance can be easily achieved by applying a gate potential, which is included in our simulations. Interestingly, a spin-polarized current can emerge as a consequence of the gate potential with the relative contribution of the two spin channels varying with the bias.

KEYWORDS: molecular electronics · ferrocene · quantum transport · electronic structure · *ab initio*

show reversible and stable hysteretic differential conductance switching.²⁰ In a seminal study, a near-perfect conduction was obtained through a ferrocene-based molecular wire.²¹ This study also revealed that the relative orientation of the five-member aromatic rings may dramatically change the conduction properties of the molecular devices. While coplanar rings lead to a large transmission probability, the relative rotation of the rings can result in a decrease of the transmission probability due to the reduced overlap between the π rings.

In this paper, we investigate the effect of another key molecular property onto the electronic transport, namely, the bonding of the end-groups to the metallic electrodes. Using spin-polarized density functional theory (DFT) combined with quantum transport, we study two- and three-terminal devices consisting of 1,1'-ferrocene dicarboxylic acid (FDCA), whose structure is illustrated in Figure 1b, sandwiched between Al(111) surfaces for different metal–molecule–metal architectures. For the two-terminal devices,

*Address correspondence to gian-marco.rignanesi@uclouvain.be.

Received for review September 10, 2009 and accepted November 17, 2009.

Published online November 24, 2009. 10.1021/nn9012059

© 2009 American Chemical Society

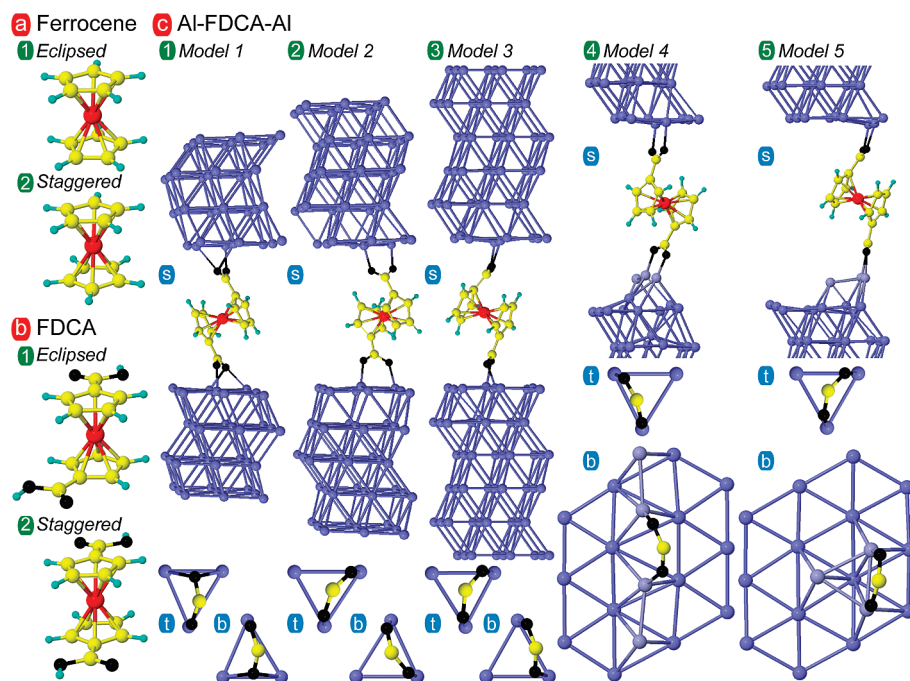


Figure 1. Ball and stick representation of (a) ferrocene, (b) FDCA, and (c) our five models of the Al-FDCA-Al system. Al, Fe, C, O, and H atoms are colored in blue, red, yellow, black, and turquoise, respectively. The two molecules (a and b) are shown in both (1) the eclipsed and (2) the staggered conformations. In models 1–3, the FDCA molecule is attached to atomically flat electrodes of Al(111); while, in models 4 and 5, the surface includes some defects (the corresponding Al atoms are colored in gray). For all five models, a side view (s) is presented. For sake of clarity, it is limited to the region where the atomic positions are relaxed, for models 4 and 5. Perpendicular views of the top (t) and bottom (b) electrodes are also reported focusing on how the COO[−] groups are attached.

we report the transmission spectra, a detailed analysis of the projected density of states (PDOS) and the current–voltage characteristics. For the three-terminal devices, we investigate the effect of the gate voltage on the transmission spectra and the current–voltage characteristics. Our calculations reveal spin-dependent transport properties at moderate negative gate voltages.

DEVICE GEOMETRY

The investigated geometries for the Al-FDCA-Al device (see Figure 1c) are built as follows. The structures of the isolated FDCA molecule and of bulk Al are first optimized. For the latter, the equilibrium lattice constant is found to be 4.19 Å, in good agreement with the experimental value. The dimension of our hexagonal supercell for the Al(111) surface is fixed based on this calculated value. To keep a minimum of about 5 Å between repeated images of the FDCA molecule, we adopt a 3 × 3 surface cell resulting in a lattice constant of 8.90 Å.

The orientation and the distance of the molecule with respect to the surface are then investigated. Various relative orientations of the O–O axis and the Al–Al bond are considered for different molecule–surface distances. In the most stable configuration, each O atom sits approximately on top of an Al atom, with the O–O axis and the Al–Al bond parallel to each other as

illustrated in Figure 1c.2,t, and the molecule–surface distance is 2.3 Å.

This is the starting point to build the full Al-FDCA-Al cell. However, this optimal molecule–surface geometry cannot always be realized. Indeed, the equilibrium structure of the FDCA is such that the two O–O axes (on opposite sides of the molecule) are parallel. Thus, the two Al(111) surfaces need to mirror each other to allow for the ideal configuration of the molecule over both the two surfaces to be realized. In general, however, this is not necessarily the case in experiments. Therefore, the ideal contact geometry should carefully be examined against other possible configurations.

It turns out that when building a periodic model for the Al-FDCA-Al structure, such nonideal situations occur quite naturally. Indeed, it is not always possible to reconcile the periodic boundary conditions,

the ABC stacking of Al, and the requirement that the two Al(111) surfaces must be mirror image of each other. This actually depends on the number of Al layers included in each electrode. The ideal configuration is obtained with five atomic layers per side (e.g., ABCAB–molecule–BCABC), while the two surfaces are necessarily different with four (e.g., BCAB–molecule–ABCA) or six (e.g., CAB CAB–molecule–CABCAB) atomic layers in each metallic contact. In what follows, the models with four, five, and six Al layers will be referred to as Model 1, Model 2, and Model 3, respectively. These three models, which are illustrated in Figure 1c.1, c.2, and c.3, are well suited as extended molecules for the transport calculations: there is no need to include more layers due to the rather short screening length in Al. The dimensions of our supercell in the direction perpendicular to the surface thus are 27.9 Å for Model 1, 32.8 Å for Model 2 and 37.4 Å for Model 3.

Realistic geometric models for molecular devices should take into account the existence of surface defects. Their influence upon the transport properties was recently emphasized for ferrocene-1,1'-dithiol inserted between Ag electrodes.²⁵ Precisely, it was pointed out that the presence of defects leads to the decrease of the molecular conductance. To investigate how the electronic transport is affected by inhomogeneities that could be present at the Al surface, two additional geometries are also generated. These are obtained by using six atomic layers in each electrode and by attaching

either a one-dimensional chain of Al atoms (Model 4) or a cluster of three additional Al atoms (Model 5) at the surface of the bottom electrode (see Figure 1c.4 and c.5). For Model 4 and Model 5, the dimension of the supercell in the direction perpendicular to the surface is identical to that of Model 3.

The final step of the cell building procedure consists in relaxing the atomic positions of the molecule and the first two atomic layers of the Al electrodes until the forces are lower than 0.04 eV/Å, while keeping the cell dimension constant and pinning the remaining atomic positions of the Al electrodes to their bulk positions. The relaxed structures can be characterized by the bonding of the molecule to the surface, the atomic displacements at the surface, and the molecular geometry deformation.

RESULTS AND DISCUSSION

In Model 1, the bonding of the molecule to the surface is considerably modified with respect to the ideal attachment. One of the O atoms still sits approximately on top of an Al atom but the second one is now located approximately in the middle of an Al–Al bond (Figure 1(c.1.t and c.1.b)). This allows for the O–O axes of FDCA to remain parallel to each other. In Model 2, the ideal configuration is obtained for both electrodes, as shown in Figure 1c.2.t and c.2.b. In Model 3, the bonding to the top electrode see Figure 1c.3.t is similar to that of Model 2, while the bonding to the bottom electrode (see Figure 1c.3.b) shows a slight rotation of the O–O axis with respect to the Al–Al bond. Finally, Models 4 and 5 present the same bonding as in Model 2 for the top electrode (see Figure 1c.4.t and c.5.t). For the bottom electrode, the bonding is illustrated in Figure 1c.4.b and c.5.b.

To quantify the distortion of the electrode surface, we compute the average displacement of the Al atoms from their bulk (initial) positions:

$$d = \frac{1}{N} \sum_{i=1}^N |\vec{r}_{i,0} - \vec{r}_{i,t}| \quad (1)$$

where N is the number of the atoms whose positions are relaxed, and $\vec{r}_{i,0}$ and $\vec{r}_{i,t}$ are the atomic positions before and after the relaxation, respectively. For the first three models, the surface distortion is found to be quite small with $d = 0.09, 0.09,$ and 0.13 Å, respectively. In Model 4, $d = 0.13$ Å for the top electrode and $d = 0.29$ Å for the bottom electrode with the one-dimensional line of Al atoms. The largest atomic displacements ($|\vec{r}_{i,0} - \vec{r}_{i,t}| = 0.84$ Å) are observed for the Al atoms which are not bonded to the O atoms. Finally, Model 5 displays the largest distortion: $d = 0.25$ Å for the top electrode and 0.33 Å for the bottom electrode containing the Al cluster. The largest atomic displacements $|\vec{r}_{i,0} - \vec{r}_{i,t}|$ are about 1 Å and occur for the two Al atoms bonded to the O atoms.

The molecular geometry deformation can be quantified by the angle between the two cyclopentane rings. After geometrical relaxation, the angle between the two cyclopentane rings is 26.6° for Model 1, 16.8° for Model 2, 10.8° for Model 3, 17.9° for Model 4, and 23.8° for Model 5. For comparison, this angle is 0° and 36° in the eclipsed and staggered forms of FDCA, respectively.

For all the models, the electronic structure is very similar for both spin components. The converged magnetic moments are negligible, ranging from 0.001 μ_B (Model 2) to 0.02 μ_B (Model 3). As a result, the computed transmission spectra, PDOS, and LDOS are almost identical for both spin components. For this reason, we only represent their sum in the sequel.

The computed transmission spectra $T(E)$ are presented in Figure 2a. The differences between the various models are not striking. The most interesting feature of $T(E)$ is that whereas several peaks are located just above the Fermi level ($E_F = 0$), very sharp peaks appear around -1.9 eV below E_F . Precisely, three peaks are present in this region. Their widths range between 0.03 eV (Model 3) and 0.07 eV (Model 1). Hereafter, we will refer to the corresponding energy windows, which are highlighted in green and yellow in Figure 2, as the LUMO and HOMO regions of the system, respectively. The reason for this abuse of language will be clear in what follows.

By comparing these transmission spectra with those obtained by Uehara *et al.*²⁶ for 1,3-ferrocenedithiolate and 1,3'-ferrocenedithiolate inserted between Au electrodes, we note two striking differences. First, the spectrum is rigidly shifted by about 2 eV to higher energies for Al–FDCA–Al. This is a direct consequence of the different chemical nature of the electrodes. Second, the transmission peaks are sharper for Al–FDCA–Al devices. This is a clear indication of a weaker metal–molecule interaction in the case of Al.

To investigate the origin of the different peaks and to explain the differences between the five models, the PDOS is computed, as reported in Figure 2b, together with the LDOS integrated over the HOMO and LUMO regions (Figure 2, panels c and d, respectively). As it can be seen from both the PDOS and the LDOS, the peaks in the HOMO region originate essentially from the atomic orbitals localized over the Fe atoms, while those in the LUMO region receive quite similar contributions from the Fe, C, and O atoms. It is interesting to distinguish the C atoms of the COO⁻ groups from those of the cyclopentane rings (C1 and C2, respectively, in the Figure 2b). While they amount to roughly the same total contribution to the PDOS in the LUMO region, the contribution *per atom* is clearly higher for the C1 atoms (since there is one C1 atom for five C2 atoms in the system), as can be seen more clearly in the LDOS. As a consequence, we expect that the COO⁻ group should play an important role in the resonant transfer at energies just above E_F .

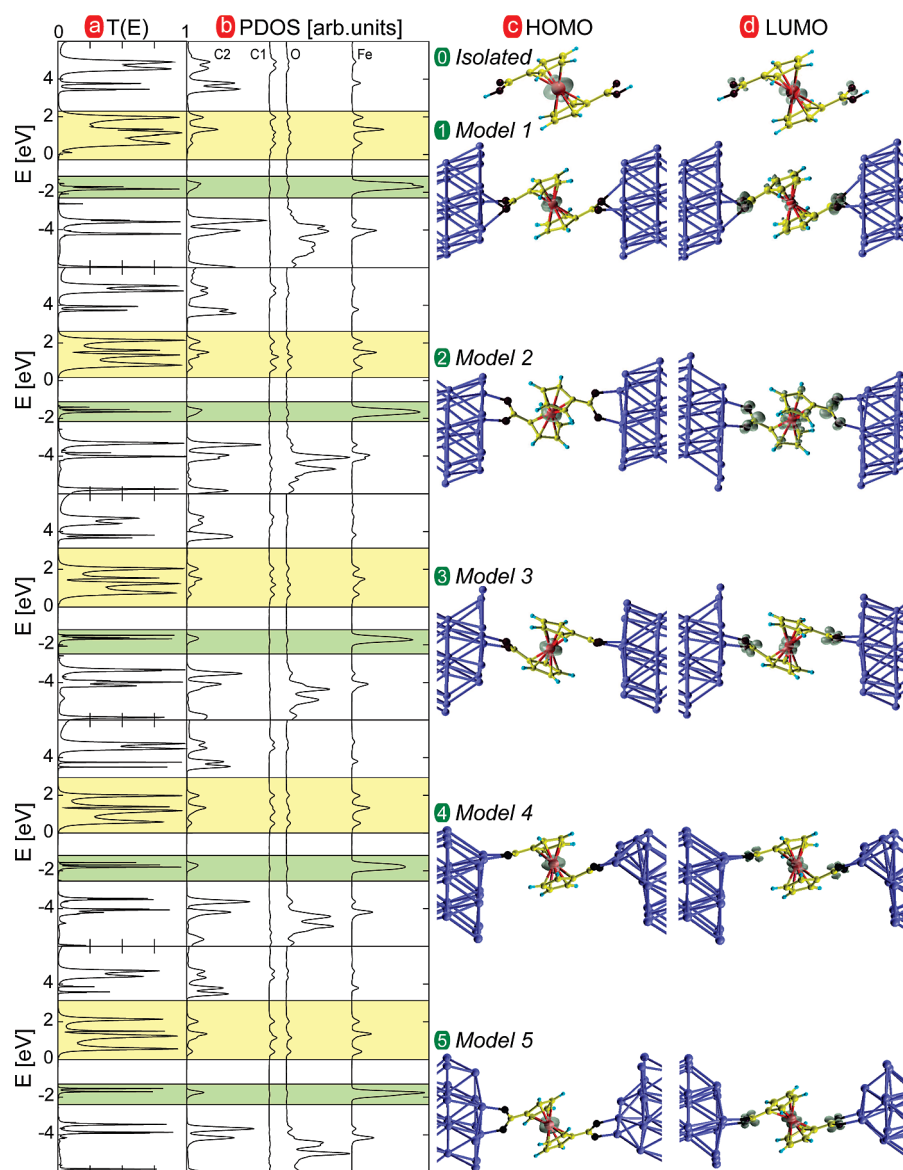


Figure 2. (a) Transmission spectra, (b) PDOS, and (c,d) LDOS for our five models (panels 1–5) of the Al–FDCA–Al system. The PDOS is presented for the different types of atoms: Fe, O, C1 (from the COO[−] groups), and C2 (from the cyclopentane rings). The LDOS is integrated over the energy windows below [(c) HOMO region highlighted in green] and above [(d) LUMO region highlighted in yellow] the Fermi level, which is set to zero. For comparison, the LDOS of the isolated FDCA molecule is also given in the panel (0) integrated (c) around HOMO, HOMO-1, and HOMO-2, and (d) around the LUMO (± 0.3 eV). The two spin contributions have been added up.

The comparison of the LDOS for Al–FDCA–Al with that of the isolated FDCA molecule suggests us the use of the terms HOMO and LUMO to label the regions of the $T(E)$ spectrum. On the one hand, the LDOS integrated around the HOMO, HOMO-1, and HOMO-2 orbitals of the FDCA, which have very similar energies and originate mainly from the states $d_{x^2-y^2}$, d_{xy} , and $d_{3z^2-r^2}$ of the Fe atom as illustrated in Figure 2c.0, is very similar to the LDOS integrated in the HOMO region of the Al–FDCA–Al device (see Figure 2c.1–5). On the other hand, the LDOS integrated around the LUMO of FDCA, which is delocalized over the Fe atom and the COOH groups (Figure

2d.0) looks very much like the LDOS integrated over the LUMO region of Al–FDCA–Al (see Figure 2d.1–5).

Next, the current–voltage (I – V) characteristics are computed for the five models. The spin-up and spin-down currents are essentially equal for biases up to 1.5 V. The maximum absolute value for the difference between the two spin-resolved currents is below 2 nA, for an average current in the μ A region. This is quite expected since the states associated to Fe are quite low in energy (around -1.9 eV) and a larger bias would be required to change their occupation. The total currents obtained by using spin polarized calculations do not differ significantly from the currents inferred in the absence of spin polarization (less than 5% difference). In what follows, we will focus only on the total current.

The I – V characteristics for the five models are illustrated in Figure 3 for biases up to 1.5 V. These differ from one model to another, proving the possibility of tuning the molecular conductance by changing the anchoring structure of the molecule to the electrodes. The lowest contact resistance is found for Model 1 while the highest is for Model 2. Interestingly, these two models are those for which the attachments of the FDCA to the Al electrodes differ the most (see Figure 1c.1.t-b and c.2.t-b), the latter being the ideal configuration of

the FDCA. In fact, it appears that the models departing the most from this ideal configuration have the lowest contact resistance, namely, Models 1, 4, and 5 (the last two being those with a defective Al surface). The potential drop in the device is found to be almost linear as illustrated for Model 3 in Figure S1 of the Supporting Information.

The I – V curves are generally quite asymmetric. The rectification coefficient $R(V) = |I(-V)/I(V)|$ is used to quantify the asymmetry. $R = 1$ means that there is no rectification of the electric current. As shown in the inset of Figure 3, we find $R < 1$ for Models 1 and 5. Interestingly, these are the ones for which

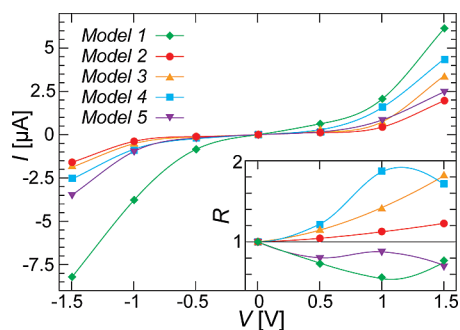


Figure 3. Current–voltage characteristics for the five models. Inset: Associated rectification coefficients as function of the voltage. The curves are obtained using spline interpolation through the points indicated on the figure for which the calculations are explicitly performed. The following symbols and colors are used: green diamonds for Model 1, red circles for Model 2, orange triangles up for Model 3, blue squares for Model 4, and violet triangles down for Model 5.

FDCA approaches the eclipsed configuration (with an angle between the two cyclopentane rings of 26.6° and 23.8°, respectively).

Our results are comparable to those obtained by Uehara *et al.*²⁶ for 1,3'-ferrocenedithiolate inserted between Au electrodes. For a bias of 1.5 V, the current ranges from 2 to 6 μA in our Al–FDCA–Al devices which is close to the $\sim 5.0 \mu\text{A}$ calculated for 1,3'-ferrocenedithiolate in contact to Au electrodes.²⁶

This proves the potential of ferrocene derivatives for the realization of robust molecular devices.

The presence of narrow peaks in the transmission spectra suggests that a precise control over the molecular conductance could be achieved in a three-terminal device thanks to a gate electrode. Therefore, we examine the I – V characteristics in the presence of a third electrode for Model 3 (see Figure 4a). This can be considered as a quite representative case, since the connection of FDCA to the Al surface is intermediate between Model 1 and Model 2. Moreover, the FDCA is closer to the staggered configuration and displays the narrowest HOMO region. The gate electrode is simulated by applying an external potential that only depends on the coordinate z perpendicular to the Al surface with the following analytical form:

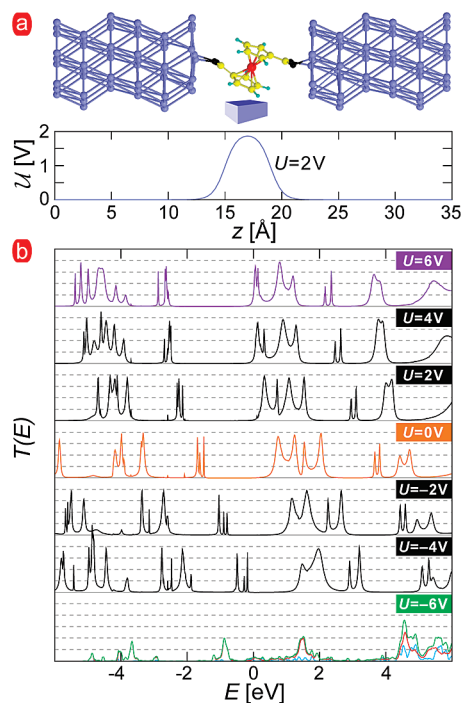


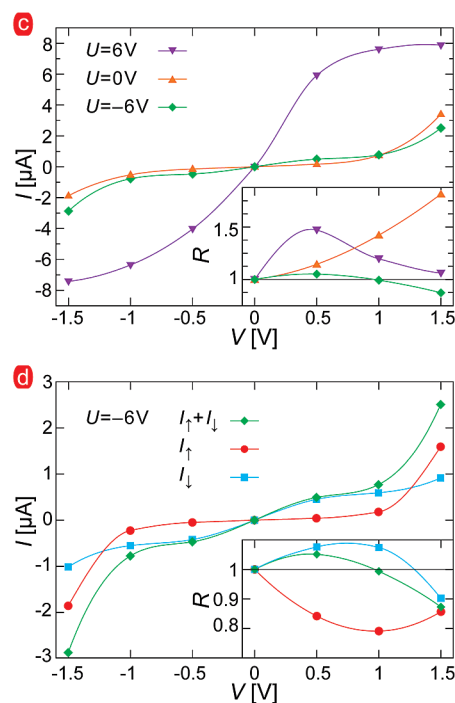
Figure 4. (a) Representation of the three-terminal device architecture based on Model 3 and the corresponding gate potential $\mathcal{U}(z)$ for an amplitude of $U = 2 \text{ V}$. (b) Transmission spectra as a function of U going from -6 to 6 V by steps of 2 V ($U = 6, 0,$ and -6 V are highlighted in violet, orange, and green, respectively). For $U = -6 \text{ V}$, the spin-up and spin-down transmission are also represented in red and blue, respectively. The Fermi level is set to zero. The dashed line indicates increments of 0.25 in the transmission. (c) Corresponding I – V curves for $U = 6 \text{ V}$ (violet triangles down), 0 V (orange triangles up), and -6 V (green diamonds) in violet, orange, and green, respectively. Inset: Associated rectification coefficients as function of the voltage. (d) Total (green diamonds), spin-up (red circles), and spin-down (blue squares) I – V curves for $U = -6 \text{ V}$. Inset: Associated rectification coefficients as function of the voltage. The curves in panels c and d are obtained using spline interpolation through the points indicated on the figure for which the calculations are explicitly performed.

$$\mathcal{U}(z) = U \left[\frac{1}{1 + e^{(z-z_1)/\Delta z}} - \frac{1}{1 + e^{(z-z_2)/\Delta z}} \right] \quad (2)$$

where $U = \pm 2, \pm 4,$ and $\pm 6 \text{ V}$ is the amplitude of the gate potential and $\Delta z = 0.5 \text{ \AA}$. Here, the parameters z_1 and z_2 control the broadening of $\mathcal{U}(z)$ (see Figure 4a). We set $z_{1/2} = z_{\text{Fe}} \pm 2.0 \text{ \AA}$, where z_{Fe} is the z coordinate of iron atom. The resulting $T(E)$ are reported in Figure 4b for various U values.

In most of the cases, the spin-up and spin-down wave functions, transmission spectra, and currents are essentially equal. But, for $U = -6 \text{ V}$, there is a clear difference between the wave functions of the two spin channels, resulting in a large magnetization of $0.46 \mu_{\text{B}}$. So, apart for this special case, we will only discuss the total transmission spectra and the total currents.

The transmission spectra are represented in Figure 4b. At low gate voltage (up to about $U = 4 \text{ V}$), the transmission peaks are essentially linearly shifted in energy as a function of U . It should be noted that the energy shift is significantly lower than the change in the gate potential: for U going from 4 to -4 V , the transmission peaks are only shifted by $\sim 2 \text{ eV}$. This can be easily understood by considering the gate potential as a perturbation to the nongated molecule. To the first order, the shift of a peak located at a given energy $E_i^{(0)}$ is simply



given by $E_i^{(1)} = \langle \psi_i^{(0)} | U | \psi_i^{(0)} \rangle$ where $\psi_i^{(0)}$ is the eigenwave function of the unperturbed system. The latter is delocalized over the entire extended molecule, and it has actually more weight on the electrodes than on the molecule itself. Its overlap with U , which acts only on the molecule (see Figure 4a), is thus quite limited, and so is the energy shift induced by U . For higher gate voltages, the shift of the HOMO and LUMO regions starts to saturate. This can be related to the fact that when $U \rightarrow -6$ V (-6 V), the LUMO (HOMO) region gets close to the Fermi level. For $U = -6$ V, the spin polarization dramatically changes the transmission spectra compared to $U = 0$ V. In particular, the transmission is considerably reduced. When the spin polarization is not taken into account for clarity, this result is not reported in Figure 4b, the HOMO region is located in the vicinity of the Fermi level. This peculiar positioning is probably the reason for the magnetization of the system. Indeed, the HOMO region corresponds essentially to atomic orbitals localized over the Fe atoms. The latter are split due to both the Stark effect and the geometry of the molecule which deviates from the D_{5d} symmetry due to the presence of COO groups and of the electrodes. As a result, the Fe atom (and hence the whole molecule) presents a spin polarization.

The I - V characteristics for $U = 0$ and ± 6 V are reported in Figure 4c for biases up to 1.5 V. For $U = 6$ V, the current is significantly enhanced due to the presence of the LUMO peaks close to the Fermi level. These orbitals are spread over the whole FDCA molecule and, therefore, they are very effective in mediating the electronic transport. For $U = -6$ V, the current is very small compared to that computed for $U = 6$ V (it is comparable to the one obtained for $U = 0$ V). This reduction is related to the drastic decrease in the transmission spectra resulting from the spin polarization. Interestingly, the current is found to be small even when the spin polarization is not taken into account (for clarity, this result is not reported in Figure 4c), despite the presence of the HOMO peaks in the vicinity of the Fermi level. It is actually smaller than that computed for $U = 0$ V. In fact, the HOMO orbitals are essentially located on the Fe atom (leading to very narrow peaks in the transmission), and hence, they are not very effective for electron transport.

METHODS

All the calculations are performed with spin-polarized DFT as implemented in the SIESTA^{27,28} and SMEAGOL^{29–31} codes. The exchange-correlation energy is evaluated using the generalized gradient approximation (GGA).³² Only valence electrons are explicitly considered and norm-conserving pseudopotentials³³ account for the core–valence interactions. The wave functions are expanded on a localized basis set:²⁷ we take a single- ζ basis set for the H, C, and O s orbitals, a double- ζ polarized basis set for Fe and the p orbitals of C and O, and a double- ζ basis set for Al. These basis sets have already been tested in previous calculations showing their accuracy.³⁴ Their overall quality is further tested in the present work by comparing the calculated

As shown in the inset of Figure 4c, the rectification coefficient is larger than 1 for both $U = 0$ V and $U = 6$ V. For $U = -6$ V, $R > 1$ at low bias voltages ($V < 1$ V) but then turns to be $R < 1$ for the higher voltages. This means that, at low voltage bias, the electron flow is easier from the FDCA end illustrated in Figure 1c.3.t toward that illustrated in Figure 1c.3.b; whereas the preferential direction is the opposite when the voltage becomes larger than 1 V.

Finally, we analyze the spin dependent transport for $U = -6$ V. The current–voltage characteristics are presented in Figure 4d. Two regions can be identified on the basis of the relative contribution of the two spin channels to the total current. At low bias ($|V| < 1.3$ V), the spin-down current (minority spins, blue line) dominates the transport, while for higher biases, the spin-up current (majority spins, red line) becomes the largest. Interestingly, the rectification coefficient R is smaller than 1 at all biases for the spin-up component; whereas, for the spin-down component, $R > 1$ for $V < 1.3$ V, and $R < 1$ at higher voltages. Note however that the deviations from $R = 1$ are much smaller than those observed previously in Figure 3 and Figure 4c.

CONCLUSIONS

In summary, we have presented *ab initio* results for FDCA molecules sandwiched between two Al(111) electrodes. Our analysis was performed using five geometrical models for the metal–molecule–metal structure. The transmission spectra and the current–voltage characteristics were calculated for these two-terminal devices. Interestingly, very sharp peaks are present in the transmission function at zero bias. In the HOMO region, these are due to resonant electron transfer through the Fe d orbitals. In contrast, in the LUMO region, atomic orbitals located on all atoms in the FDCA are involved in the resonant transfer. While the computed current–voltage characteristics are asymmetric and spin-independent in two-terminal devices, spin effects can be obtained in three-terminal devices for moderate negative gate potentials. Remarkably, the contribution of the two spin channels to the total current depends on the applied bias.

structure of eclipsed ferrocene (D_{5h}) to the experimental measurements.³⁵ First-principles simulations using a plane-wave expansion are also performed with ABINIT³⁶ allowing us to monitor the convergence of the results with respect to the basis set size. The typical bond lengths computed with the localized basis sets and with the plane-wave expansion differ by less than 1%, and deviate by at most 2% from the experimental values. The energy barrier between the eclipsed and staggered conformations is found to be 0.034 eV with the localized basis sets and 0.040 eV using the plane-wave expansion.

We use periodic boundary conditions in the direction orthogonal to the transport direction, sampling over a uniform 3×3 grid of k -points in the two-dimensional Brillouin zone. In the transport

calculations, the Green's function leading to the density matrix is integrated typically over 32 energy points on the complex semi-circle, 32 points along the line parallel to the real axis, and 16 poles. The integral over real energies necessary at finite bias is evaluated over at least 800 points. The real-space grid cutoff was chosen to give an equivalent plane-wave energy cutoff of 300 Ry.

Acknowledgment. The work was supported by the Belgian FRS–FNRS and the TINTIN and NANOMOL projects [“Actions de Recherches Concertées - Communauté Française de Belgique”]. All the calculations were done at CISM, Université Catholique de Louvain, in the frame of the project FRFC No. 2.4502.05 “Simulation numérique. Applications en physique de l'état solide, océanographie et dynamique des fluides.” S.S., I.R., and A.R.R. wish to thank Science Foundation of Ireland (Grants: SFI07/RFP/PHYF235 and SFI/07/IN.1/1945). The SMEAGOL project is supported by Science Foundation of Ireland.

Supporting Information Available: The difference ΔV_H between the planar average of the Hartree potential at a given bias ($V = 0.5, 1.0, \text{ and } 1.5 \text{ V}$) and that at zero bias; it is constant in the leads and drops almost linearly in between (on the molecule). This material is available free of charge via the Internet at <http://pubs.acs.org>.

REFERENCES AND NOTES

- Aviram, A.; Ratner, M. A. Molecular Rectifiers. *Chem. Phys. Lett.* **1974**, *29*, 277–283.
- Datta, S. *Electron Transport in Mesoscopic Systems*; Cambridge University Press: Cambridge, 1997.
- Di Ventra, M.; Pantelides, S. T.; Lang, N. D. First-Principles Calculation of Transport Properties of a Molecular Device. *Phys. Rev. Lett.* **2000**, *84*, 979–982.
- Magoga, M.; Joachim, C. Conductance of Molecular Wires Connected or Bonded in Parallel. *Phys. Rev. B* **1999**, *59*, 16011–16021.
- Taylor, J.; Brandbyge, M.; Stokbro, K. Theory of Rectification in Tour Wires: The Role of Electrode Coupling. *Phys. Rev. Lett.* **2002**, *89*, 138301.
- Potember, R. S.; Poehler, T. O.; Cowan, D. O. Electrical Switching and Memory Phenomena in Cu-TCNQ Thin Films. *Appl. Phys. Lett.* **1979**, *34*, 405–407.
- Reed, M. A.; Zhou, C.; Muller, C. J.; Burgin, T. P.; Tour, J. M. Conductance of a Molecular Junction. *Science* **1997**, *278*, 252–254.
- Tour, J. M. Molecular Electronics. Synthesis and Testing of Components. *Acc. Chem. Res.* **2000**, *33*, 791–804.
- Collier, C. P.; Mattersteig, G.; Wong, E. W.; Luo, Y.; Beverly, K.; Sampaio, J.; Raymo, F. M.; Stoddart, J. F.; Heath, J. R. A [2]Catenane-Based Solid State Electronically Reconfigurable Switch. *Science* **2000**, *289*, 1172–1175.
- Moth-Poulsen, K.; Bjørnholm, T. Molecular Electronics with Single Molecules in Solid-State Devices. *Nat. Nanotechnol.* **2009**, *4*, 551–556.
- Salomon, A.; Cahen, D.; Lindsay, S.; Tomfohr, J.; Engelkes, V. B.; Frisbie, C. D. Comparison of Electronic Transport Measurements on Organic Molecules. *Adv. Mater.* **2003**, *15*, 1881–1890.
- Li, Q.; Surthi, S.; Mathur, G.; Gowda, S.; Zhao, Q.; Sorenson, T. A.; Tenent, R. C.; Muthukumaran, K.; Lindsey, J. S.; Misra, V. Multiple-Bit Storage Properties of Porphyrin Monolayers on SiO₂. *Appl. Phys. Lett.* **2004**, *85*, 1829–1831.
- Engtrakul, C.; Sita, L. R. Ferrocene-Based Nanoelectronics: 2,5-Diethynylpyridine as a Reversible Switching Element. *Nano Lett.* **2001**, *1*, 541–549.
- Jiao, J.; Long, G. J.; Grandjean, F.; Beatty, A. M.; Fehner, T. P. Building Blocks for the Molecular Expression of Quantum Cellular Automata. Isolation and Characterization of a Covalently Bonded Square Array of Two Ferrocenium and Two Ferrocene Complexes. *J. Am. Chem. Soc.* **2003**, *125*, 7522–7523.
- Park, J.; Pasupathy, A. N.; Goldsmith, J. I.; Chang, C.; Yaish, Y.; Petta, J. R.; Rinkoski, M.; Sethna, J. P.; Abruna, H. D.; McEuen, P. L.; Ralph, D. C. Coulomb Blockade and the Kondo Effect in Single-Atom Transistors. *Nature* **2002**, *417*, 722–725.
- Kornilovitch, P. E.; Bratkovsky, A. M.; Williams, R. S. Bistable Molecular Conductors with a Field-Switchable Dipole Group. *Phys. Rev. B* **2002**, *66*, 245413.
- Coriani, S.; Haaland, A.; Jørgensen, P. The Equilibrium Structure of Ferrocene. *ChemPhysChem* **2006**, *7*, 245–249.
- Long, N. *Metalloenes. An Introduction to Sandwich Complexes*; Blackwell Science Ltd.: London, 1998.
- Wassel, R. A.; Credo, G. M.; Fuierer, R. R.; Feldheim, D. L.; Gorman, C. B. Attenuating Negative Differential Resistance in an Electroactive Self-Assembled Monolayer-Based Junction. *J. Am. Chem. Soc.* **2004**, *126*, 295–300.
- Dinglasan, J. A. M.; Bailey, M.; Park, J. B.; Dhirani, A.-A. Differential Conductance Switching of Planar Tunnel Junctions Mediated by Oxidation/Reduction of Functionally Protected Ferrocene. *J. Am. Chem. Soc.* **2004**, *126*, 6491–6497.
- Getty, S. A.; Engtrakul, C.; Wang, L.; Liu, R.; Ke, S.-H.; Baranger, H. U.; Yang, W.; Fuhrer, M. S.; Sita, L. R. Near-Perfect Conduction Through a Ferrocene-Based Molecular Wire. *Phys. Rev. B* **2005**, *71*, 241401(R).
- Liu, R.; Ke, S.-H.; Baranger, H. U.; Yang, W. Organometallic Spintronics: Dicobaltocene Switch. *Nano Lett.* **2005**, *5*, 1959–1962.
- Shen, X.; Yi, Z.; Shen, Z.; Zhao, X.; Wu, J.; Hou, S.; Sanvito, S. The Spin Filter Effect of Iron-Cyclopentadienyl Multidecker Clusters: The Role of the Electrode Band Structure and the Coupling Strength. *Nanotechnology* **2009**, *20*, 385401.
- Wang, L.; Cai, Z.; Wang, J.; Lu, J.; Luo, G.; Lai, L.; Zhou, J.; Qin, R.; Gao, Z.; Yu, D.; Li, G.; Mei, W. N.; Sanvito, S. Novel One-Dimensional Organometallic Half Metals: Vanadium–Cyclopentadienyl, Vanadium–Cyclopentadienyl–Benzene, and Vanadium–Anthracene Wires. *Nano Lett.* **2008**, *8*, 3640–3644.
- Bredow, T.; Tegenkamp, C.; Pfnür, H.; Meyer, J.; Maslyuk, V. V.; Mertig, I. Ferrocene–1,1'-Dithiol as Molecular Wire between Ag Electrodes: The Role of Surface Defects. *J. Chem. Phys.* **2008**, *128*, 064704.
- Uehara, T.; Belosludov, R. V.; Farajian, A. A.; Mizuseki, H.; Kawazoe, Y. Electronic and Transport Properties of Ferrocene: Theoretical Study. *Jpn. J. Appl. Phys.* **2006**, *45*, 3768–3771.
- Ordejon, P.; Artacho, E.; Soler, J. M. Self-Consistent Order-N Density-Functional Calculations for Very Large Systems. *Phys. Rev. B* **1996**, *53*, R10441–R10444.
- Soler, J. M.; Artacho, E.; Gale, J. D.; Garcia, A.; Junquera, P.; Ordejon, P. The SIESTA Method for *ab Initio* Order-N Materials Simulation. *J. Phys.: Condens. Mater.* **2002**, *14*, 2745–2779.
- Rocha, A. R.; Garcia-Suarez, V.; Bailey, S. W.; Lambert, C. J.; Ferrer, J.; Sanvito, S. Towards Molecular Spintronics. *Nat. Mater.* **2005**, *4*, 335–339.
- Rocha, A. R.; Garcia-Suarez, V.; Bailey, S. W.; Lambert, C. J.; Ferrer, J.; Sanvito, S. Spin and Molecular Electronics in Atomically Generated Orbital Landscapes. *Phys. Rev. B* **2006**, *73*, 085414.
- Rungger, I.; Sanvito, S. Algorithm for the Construction of Self-Energies for Electronic Transport Calculations Based on Singularity Elimination and Singular Value Decomposition. *Phys. Rev. B* **2008**, *78*, 035407.
- Perdew, J. P.; Burke, K.; Ernzerhof, M. Generalized Gradient Approximation Made Simple. *Phys. Rev. Lett.* **1996**, *77*, 3865–3868.
- Troullier, N.; Martins, J. L. Efficient Pseudopotentials for Plane-Wave Calculations. *Phys. Rev. B* **1992**, *46*, 1754–1765.
- Ozaki, T.; Kino, H. Numerical Atomic Basis Orbitals from H to Kr. *Phys. Rev. B* **2004**, *69*, 195113.
- Haaland, A.; Nilsson, J. Determination of Barriers to Internal Rotation by Means of Electron Diffraction. Ferrocene and Ruthenocene. *Acta Chem. Scand.* **1968**, *22*, 2653–2670.
- Gonze, X.; Beuken, J.-M.; Caracas, R.; Detraux, F.; Fuchs, M.; Rignanese, G.-M.; Sindic, L.; Verstraete, M.; Zerah, G.; Jollet, F.; *et al.* First-Principles Computation of Material Properties: the ABINIT Software Project. *Comput. Mater. Sci.* **2002**, *25*, 478–492. <http://www.abinit.org>.